Frontiers in Bioscience Landmark

Front. Biosci. (Landmark Ed) **2026**; 31(11): 55718
https://doi.org/10.31083/FBL55718

Original Research

SEMA3C Is Upregulated in Liver Fibrosis and Serves as a Pan-Cancer Prognostic Biomarker Correlated With CAF Infiltration: An Experimental and Multi-Omics Study

Xiaoxin Zhang[1,2,3,*], Qian Hu[2], Yongli Huang[2], Chengdong Liang[2], Tiancheng Shen[2], Maoye Wang[2], Changlei Ning[2], Gong Guo[2], Jiahui Zhang[2], Runbi Ji[2], Min Fu[2], Xu Zhang[1,2,*]

[1]School of Basic Medical Science and Public Health, Jiangsu University, 212013 Zhenjiang, Jiangsu, China
[2]Jiangsu Key Laboratory of Medical Science and Laboratory Medicine, Jiangsu University, 212013 Zhenjiang, Jiangsu, China
[3]Department of Pathology, Li Ka Shing Faculty of Medicine, The University of Hong Kong, Hong Kong, China
*Correspondence: zhangxiaoxin2014@163.com (Xiaoxin Zhang); xuzhang@ujs.edu.cn (Xu Zhang)
Academic Editor: Guor Mour Her
Submitted: 7 July 2026 Revised: 22 September 2026 Accepted: 15 October 2026 Published: 17 November 2026

Abstract

Background: Liver fibrosis, characterized by excessive extracellular matrix (ECM) deposition following chronic injury, is a pivotal step toward cirrhosis and hepatocellular carcinoma and represents a major global health burden associated with aberrant stromal remodeling. This study aimed to investigate the role of semaphorin 3C (*SEMA3C*) in liver fibrosis and its pan-cancer prognostic significance, focusing on its function within the fibrotic–neoplastic axis of stromal dynamics. **Methods:** Integrated multi-omics analyses of public datasets (Gene Expression Omnibus [GEO] and The Cancer Genome Atlas [TCGA]) were combined with experimental validation in human and rodent fibrotic liver tissues. *SEMA3C* expression was assessed by transcriptomic profiling and immunohistochemistry, and its cellular localization was examined in mouse and rat models of liver fibrosis. Functional studies employed siRNA-mediated knockdown in LX-2 cells, with assessments of fibrotic marker expression and cell migration. Pan-cancer analyses across multiple malignancies evaluated SEMA3C expression, associations with overall survival (OS), diagnostic accuracy (AUC), TME composition, and pathway enrichment. Genomic drivers of SEMA3C dysregulation were investigated through copy number variation (CNV) and DNA methylation analyses. **Results:** *SEMA3C* was significantly upregulated in fibrotic livers from both human and rodent samples, with expression levels correlating with fibrosis severity. In mouse and rat liver fibrosis models, immunofluorescence showed that *SEMA3C* co-localized predominantly with activated hepatic stellate cells (HSCs). In LX-2 cells, *SEMA3C* knockdown reduced fibrotic marker expression and suppressed migration. Pan-cancer analysis revealed widespread SEMA3C overexpression across multiple tumor types, which was associated with poor OS and promising diagnostic accuracy (AUC up to 0.946). *SEMA3C* expression was positively correlated with cancer-associated fibroblast (CAF) infiltration, ECM organization, and epithelial–mesenchymal transition. Copy number amplifications and promoter hypomethylation were identified as potential mechanisms underlying *SEMA3C* upregulation. **Conclusion:** *SEMA3C* is consistently upregulated in liver fibrosis and across diverse cancers, with expression levels associated with fibrosis severity, poor prognosis, and stromal remodeling. These findings identify SEMA3C as a candidate diagnostic and prognostic biomarker and suggest a potential role in ECM remodeling at the fibrotic–neoplastic interface. Future studies should validate its functions *in vivo* and explore therapeutic strategies targeting *SEMA3C* signaling.

Keywords: semaphorins; liver fibrosis; neoplasms; tumor microenvironment; cancer-associated fibroblasts; biomarkers

1. Introduction

Liver fibrosis represents a pivotal pathological process characterized by excessive deposition of extracellular matrix (ECM) following chronic liver injury, serving as a critical intermediary stage bridging various chronic liver diseases—such as viral hepatitis, alcohol-related liver disease, and non-alcoholic fatty liver disease (NAFLD)—to cirrhosis, liver failure, and hepatocellular carcinoma (HCC) [1]. This condition creates a substantial global health burden, contributing significantly to rising morbidity and mortality rates. Current therapeutic strategies are largely limited to managing underlying etiologies and providing supportive care. While liver transplantation remains the only curative option for end-stage patients, its clinical utility is heavily constrained by donor scarcity and high financial costs [2]. Hence, unraveling the molecular drivers of fibrogenesis is imperative to discover innovative diagnostic biomarkers and therapeutic targets for this unresolved clinical challenge.

This growing global health burden highlights the urgent need for further research. Chronic liver diseases are a growing epidemic worldwide, with NAFLD alone affecting approximately 25% of the global population and serving as a leading cause of liver fibrosis [3]. The progres-

Copyright: © 2026 The Author(s). Published by IMR Press.
This is an open access article under the CC BY 4.0 license.

Publisher's Note: IMR Press stays neutral with regard to jurisdictional claims in published maps and institutional affiliations.

sion from simple steatosis to steatohepatitis, and eventually to advanced fibrosis and cirrhosis, is a dynamic process driven by complex cellular crosstalk and impaired tissue repair. During this pathological process, the activation of HSCs into proliferative myofibroblasts is a central event that leads to excessive ECM deposition [4]. Chronically injured hepatocytes and immune cells release potent cytokines, among which transforming growth factor-beta 1 (TGF-β1) represents the canonical master regulator that triggers downstream SMAD2/3 phosphorylation to activate HSCs [5]. Additionally, classical pathways such as the Wnt/β-catenin, Hedgehog, and platelet-derived growth factor (PDGF) signaling cascades closely cooperate to sustain myofibroblast proliferation and survival [6]. In recent years, breakthrough studies have expanded this landscape beyond traditional fibrogenic factors, identifying novel regulators of stromal activation, including enzymes, epigenetic modifiers and cytokines [7,8]. In addition, the clinical management of liver fibrosis has increasingly focused on identifying reliable biomarkers, particularly secretable proteins that indicate fibrosis progression. Conventional laboratory panels rely on indirect biomarkers, such as APRI and FIB-4 [9], whereas direct secretory biomarkers, including HA, TIMP-1, and type IV collagen, reflect matrix dynamics [10]. However, because these circulating markers largely represent downstream products of matrix turnover, they are highly susceptible to systemic metabolic clearance and frequently lack sufficient sensitivity for detecting early-stage fibrosis [10,11]. This limitation underscores the need to identify novel upstream secretory signaling molecules that directly reflect the activation of fibrosis.

Recent research has expanded beyond canonical fibrogenic pathways to explore the roles of axon guidance molecules, which were originally known for nerve development but have now been recognized for their critical functions in tissue remodeling, such as Netrin-1, Slit2, and various semaphorin members including SEMA7A [12,13,14]. These molecules have emerged as important regulators of cell movement and matrix structures in both organ fibrosis and cancer [15]. Semaphorins, initially characterized by their role in neuronal development, are now recognized as pivotal regulators of immune responses, angiogenesis, and the tumor microenvironment (TME) remodeling [16]. Among them, secreted class-3 semaphorins (SEMA3s) have attracted considerable interest and have been implicated in promoting tumor progression in various cancers, including pancreatic, gastric, and lung carcinomas, through mechanisms involving enhanced cell proliferation, invasion, and modulation of the stromal compartment [17,18]. Within the TME, CAFs actively orchestrate tumor progression, ECM remodeling, and therapeutic resistance [19]. Activated CAFs deposit dense collagen networks and secrete MMPs to facilitate cancer cell invasion and metastasis. Recent evidence also highlights that CAFs mediate complex cell-to-cell communication within the tumor microenvironment, transferring diverse functional components to sustain tumor progression [20,21]. Consequently, identifying the regulators of CAF presence and stromal reactivation is essential for developing targeted interventions. Notably, these functions of *SEMA3C*, such as influencing cell migration, ECM organization, and stromal cell activation, are highly consistent with the key pathological features of liver fibrosis. These findings suggest that SEMA3C may play a common regulatory role in both tissue fibrosis and stroma-rich tumors. However, its specific expression and function in liver fibrosis, as well as its broader pan-cancer clinical significance, have not been systematically investigated.

To address these questions, this study first investigated the role of *SEMA3C* in liver fibrosis by combining bioinformatics analysis with extensive experimental validation. Using clinical tissues, tissue microarrays (TMAs), and cell models, we verified the upregulation of *SEMA3C* in fibrotic livers, identified its cellular localization in activated HSCs in rodent models of liver fibrosis, and demonstrated that its knockdown suppresses LX-2 cell migration and fibrotic marker expression. We then extended our analysis to a pan-cancer scale using The Cancer Genome Atlas (TCGA) datasets to systematically evaluate the expression, genetic alterations, and clinical significance of SEMA3C across multiple malignancies, particularly focusing on its correlation with CAF infiltration. Overall, this study aims to clarify the pro-fibrotic function of *SEMA3C* and uncover its potential value as a pan-cancer biomarker.

2. Materials and Methods

2.1 Clinical Samples and qPCR Validation

Human liver specimens were collected from patients treated at Renji Hospital, Shanghai Jiao Tong University School of Medicine between 2010 and 2015, and were analysed retrospectively. The cohort comprised liver fibrosis tissues (n = 5) and normal liver control tissues (n = 7). Group allocation was based on the histological diagnosis issued by the hospital pathology service: specimens with established cirrhosis were assigned to the fibrosis group, whereas histologically normal liver tissues lacking fibrosis and significant necroinflammatory activity were assigned to the normal control group. The fibrotic specimens corresponded to end-stage fibrosis (METAVIR F4; Ishak stage 5–6), and no specimen with intermediate-stage fibrosis was included. The cirrhotic cases were of mixed etiology, predominantly viral hepatitis and alcohol-related liver disease; because the original clinical records were not systematically annotated by etiology, the cases were not further stratified into etiological subtypes. Written informed consent was obtained from all patients, and the study was approved by the Hospital Ethics Committee (KY2016-075-A). Total RNA was extracted from clinical liver fibrosis tissues and normal liver controls using TRIzol reagent (catalogue no. 15596026; Invitrogen, Thermo Fisher Scientific,

Carlsbad, CA, USA). RNA concentration and purity were measured with a NanoDrop spectrophotometer (ND-2000, Thermo Fisher Scientific, Waltham, MA, USA), with the A260/A280 ratio required to fall between 1.8 and 2.0. Total RNA (1 µg) was reverse transcribed into cDNA using a PrimeScript™ RT Reagent Kit (catalogue no. RR037A; Takara Bio, Kusatsu, Shiga, Japan) according to the manufacturer's protocol. Real-time PCR analysis was conducted using SYBR Premix Ex Taq II (Tli RNaseH Plus; catalogue no. RR420A; Takara Bio, Kusatsu, Shiga, Japan) on a 7500 Real-Time PCR System (Applied Biosystems, Thermo Fisher Scientific, Foster City, CA, USA). Relative *SEMA3C* mRNA expression was calculated using the $2^{-\Delta\Delta Ct}$ method, with GAPDH serving as the endogenous reference gene. All reactions were performed in triplicate. Primer sequences are listed in Table 1.

Table 1. Sequences of primers used for real-time PCR.

Primer	Sequence 5′-3′
SEMA3C Forward	ATTCAGACTTTCAATCGCACACA
SEMA3C Reverse	ACAGACACCGTGTTCACGTTG
GAPDH Forward	CTGGGCTACACTGAGCACC
GAPDH Reverse	AAGTGGTCGTTGAGGGCAATG

SEMA3C, semaphorin 3C; *GAPDH*, glyceraldehyde-3-phosphate dehydrogenase.

2.2 TMA and Immunohistochemistry (IHC)

TMAs were purchased from Xi'an Alena Biotechnology Ltd. Co. (catalogue no. LV805a; Xi'an, Shaanxi, China), and the relevant clinical data were provided by the company. As the commercially obtained TMAs are fully de-identified and their use does not involve identifiable human subjects, the use of these samples was exempt from additional ethical review. The TMA block was constructed from formalin-fixed, paraffin-embedded (FFPE) tissue blocks and contained 80 cases with a single 1.5-mm core per case. Group assignment followed the pathological diagnosis recorded for each case by the supplier's certified pathologist: 30 cases of cancer-adjacent histologically normal hepatic tissue were designated as the normal group, 10 cases of chronic hepatitis constituted the inflammation group, and 40 cases of hepatic cirrhosis constituted the liver fibrosis group. The three groups were therefore defined by histological diagnosis rather than by a numerical fibrosis stage: the liver fibrosis group corresponds to end-stage fibrosis (METAVIR F4; Ishak stage 5–6), whereas the inflammation group represents chronic necroinflammatory injury without established cirrhosis. The etiology of the hepatitis and cirrhosis cases was not annotated in the supplier's datasheet, and etiology-stratified analysis was therefore not performed. The complete case-level annotation of the array, including age, sex, organ, pathological diagnosis and assigned group for all 80 cases, is provided in **Supplementary Table 1**. Sections (5 µm) were prepared from the TMA blocks. After xylene deparaffinization and graded ethanol rehydration, antigens were retrieved in citrate buffer (pH 6.0) at 95 °C for 20 min. Endogenous peroxidase was blocked with 3% hydrogen peroxide (Sigma-Aldrich, St. Louis, MO, USA) for 10 min, followed by 5% normal goat serum (Jackson ImmunoResearch, West Grove, PA, USA) for 1 h at room temperature to inhibit non-specific binding. Then, sections were incubated with a primary antibody against *SEMA3C* (catalogue no. 30638-1-AP; Proteintech, Rosemont, IL, USA; 1:300 dilution) overnight at 4 °C. After washing, the sections were incubated with HRP-conjugated secondary antibody (catalogue no. RGAR001; Proteintech, Rosemont, IL, USA) for 30 min at room temperature. Signal was developed using a 3,3′-diaminobenzidine (DAB) substrate kit (catalogue no. D5637; Sigma-Aldrich, St. Louis, MO, USA), and counterstaining was performed with Mayer's hematoxylin (Sigma-Aldrich, St. Louis, MO, USA). Staining intensity was semi-quantitatively evaluated by two independent pathologists unaware of clinical data, considering both the percentage of positive cells (0: <5%; 1: 5–25%; 2: 26–50%; 3: 51–75%; 4: >75%) and staining strength (0: negative; 1: weak; 2: moderate; 3: strong); the product of these two scores generated a final immunoreactivity value ranging from 0 to 12, which was subsequently stratified into low (0–4), medium (5–8), and high (9–12) expression categories.

2.3 Immunofluorescence Staining and Co-Localization Analysis

To determine the cellular localization of *SEMA3C* in fibrotic liver, immunofluorescence staining was performed on FFPE sections of fibrotic liver tissues from carbon tetrachloride (CCl_4)-induced mouse and rat models. To establish the liver fibrosis models, male C57BL/6 mice (6–8 weeks old, n = 5 per group) and male Sprague-Dawley (SD) rats (6–8 weeks old, n = 5 per group) were randomized into control and model groups. For the mouse model, liver fibrosis was induced by intraperitoneal injection of 10% CCl_4 (dissolved in olive oil) at a dose of 2 mL/kg body weight, twice a week for 6 consecutive weeks. For the rat model, rats received intraperitoneal injections of 50% CCl_4 (also dissolved in olive oil) at a dose of 2 mL/kg body weight (approximately 1.0 mL/kg calculated as pure CCl_4), twice a week (with an interval of approximately 3–4 days) for 8 consecutive weeks. Animals in the respective control groups received equivalent volumes of olive oil alone. All animal procedures were approved by the Institutional Animal Care and Use Committee of Jiangsu University (approval no. UJS-IACUC-2025031646) and were performed in accordance with the Guidelines for Ethical Review of Animal Welfare (GB/T 35892-2018, National Standards of the People's Republic of China) and the Guide for the Care and Use of Laboratory Animals (8th edition, National Research Council, USA), together with the Regulations on the

Administration of Laboratory Animals of the People's Republic of China (State Council, revised 2017). The study is reported in accordance with the ARRIVE 2.0 guidelines. Animals were anesthetized with 2%–4% isoflurane inhalation, and deep anesthesia was confirmed by the loss of the toe-pinch reflex before tissue harvesting. Animals were euthanized by prolonged exposure to 5% isoflurane until cardiac and respiratory arrest was confirmed.

Sections (4 μm) were deparaffinized, rehydrated, and subjected to heat-induced antigen retrieval in sodium citrate buffer (pH 6.0) at 95 °C for 20 min. After blocking with 5% donkey serum (Jackson ImmunoResearch, West Grove, PA, USA) in phosphate-buffered saline (PBS; pH 7.4) containing 0.1% Triton X-100 (Sigma-Aldrich, St. Louis, MO, USA) for 1 h at room temperature, sections were co-incubated overnight at 4 °C with primary antibodies against SEMA3C (catalogue no. 30638-1-AP; Proteintech, Rosemont, IL, USA; 1:300 dilution) and the HSC activation marker α-SMA (catalogue no. 67735-1-Ig; Proteintech, Rosemont, IL, USA; 1:300). After washing three times with PBS, the sections were incubated for 1 h at room temperature with species-specific fluorescence-conjugated secondary antibodies Alexa Fluor 488 donkey anti-rabbit IgG (H+L), catalogue no. A-21206, and Alexa Fluor 594 donkey anti-mouse IgG (H+L), catalogue no. A-21203, both Highly Cross-Adsorbed; Thermo Fisher Scientific, Waltham, MA, USA; 1:500 dilution for both. Nuclei were counterstained with DAPI (1 μg/mL; catalogue no. D9542; Sigma-Aldrich, St. Louis, MO, USA). Coverslips were mounted using an anti-fade mounting medium (Sigma-Aldrich, St. Louis, MO, USA), and images were acquired on an LSM 880 confocal laser scanning microscope (Carl Zeiss AG, Oberkochen, Germany).

2.4 Cell Culture and siRNA Transfection

The human HSCs line LX-2 was originally obtained from Shanghai Cancer Institute (Shanghai, China). The cell line was formally authenticated using Short Tandem Repeat (STR) profiling and was routinely screened to confirm the absence of mycoplasma contamination before use. The LX-2 cells were cultured in Dulbecco's Modified Eagle's Medium (DMEM; catalogue no. 11965092; Gibco, Thermo Fisher Scientific, Waltham, MA, USA) supplemented with 10% fetal bovine serum (catalogue no. 10099141; Gibco, Thermo Fisher Scientific, Waltham, MA, USA) and 1% penicillin–streptomycin (catalogue no. 15140122; Gibco, Thermo Fisher Scientific, Waltham, MA, USA) at 37 °C in a humidified atmosphere containing 5% CO_2.

Small interfering RNAs (siRNAs) targeting *SEMA3C* and a non-targeting negative control siRNA were designed and synthesized by GenePharma (Shanghai, China). The sequences of the three *SEMA3C*-specific siRNAs were as follows (sense/antisense, 5′→3′): si-*SEMA3C*-1, CCUAUGUUUGUAGAUGCACdTdT/GUGCAUCUACAAACAUAGGdTdT; si-*SEMA3C*-2, CGUGUAAUUCAGACUUUCAdTdT/UGAAAGUCUGAAUUACACGdTdT; si-*SEMA3C*-3, GCCCUCAUCAAUAGUCGGAdTdT/UCCGACUAUUGAUGAGGGCdTdT. The non-targeting negative control siRNA was obtained from the same manufacturer. For transfection, LX-2 cells were seeded in 6-well plates at a density of 2×10^5 cells per well and cultured overnight to reach approximately 60–70% confluence. siRNAs were transfected at a final concentration of 50 nM using Lipofectamine RNAiMAX (catalogue no. 13778150; Invitrogen, Thermo Fisher Scientific, Carlsbad, CA, USA) according to the manufacturer's instructions. After 6 h of incubation, the transfection medium was replaced with fresh complete medium. Cells were harvested at 48 h post-transfection for subsequent RNA or protein extraction. All three SEMA3C-specific siRNAs were screened for knockdown efficiency by quantitative real-time PCR and western blot. si-SEMA3C-1 and si-SEMA3C-2 produced the greatest reduction in SEMA3C expression and were both used in the subsequent experiments.

2.5 Transwell Migration Assay

Cell migration was assessed using Transwell® Permeable Supports(8 μm pore size; catalogue no. 3422; Corning Incorporated, Corning, NY, USA). Following siRNA transfection (48 h), LX-2 cells were trypsinized, washed twice with PBS, and resuspended in serum-free DMEM. A total of 4×10^4 cells in 200 μL of serum-free medium were seeded into the upper chamber. The lower chamber was filled with 700 μL of DMEM supplemented with 20% fetal bovine serum as a chemoattractant. After incubation at 37 °C in a 5% CO_2 humidified incubator for 24 h, the medium was removed, and cells on the upper surface of the membrane were gently wiped off with a cotton swab. The migrated cells on the lower surface were fixed with 4% paraformaldehyde (Sigma-Aldrich, St. Louis, MO, USA) for 15 min and stained with 0.1% crystal violet (Sigma-Aldrich, St. Louis, MO, USA) for 20 min. The membranes were washed with PBS, air-dried, and photographed under an IX73 inverted microscope (Olympus, Tokyo, Japan). Five randomly selected fields per membrane were counted at 200× magnification. Each experiment was performed in triplicate.

2.6 Western Blot

Total protein was extracted from cells using RIPA lysis buffer(catalogue no. 89900; Thermo Fisher Scientific, Waltham, MA, USA) supplemented with protease and phosphatase inhibitor cocktails (catalogue nos. 05892791001 and 04906837001; Roche Diagnostics, Mannheim, Germany). Protein concentrations were determined using the Bradford assay (catalogue no. 5000006; Bio-Rad Laboratories, Hercules, CA, USA) with bovine serum albumin (Sigma-Aldrich, St. Louis, MO, USA) as a standard. Equal amounts of protein (30 μg/lane) were resolved by sodium dodecyl sulfate-polyacrylamide gel elec-

trophoresis (SDS-PAGE) on 10% gels and transferred onto polyvinylidene fluoride (PVDF) membranes (catalogue no. 10600023; Amersham, Cytiva, Marlborough, MA, USA) using a Trans-Blot Turbo transfer system (Bio-Rad Laboratories, Hercules, CA, USA). Membranes were blocked with 5% non-fat milk in Tris-buffered saline containing 0.1% Tween-20 (TBST) for 1 h at room temperature, then incubated overnight at 4 °C with the following primary antibodies diluted in blocking buffer: SEMA3C (catalogue no. 87702-1-RR; 1:1000), α-SMA (catalogue no. 67735-1-Ig; 1:1000), vimentin (catalogue no. 10366-1-AP; 1:20,000) and β-actin (catalogue no. 66009-1-Ig; 1:20,000), all from Proteintech (Rosemont, IL, USA). After washing three times with TBST, membranes were incubated with horseradish peroxidase-conjugated secondary antibodies (anti-rabbit, catalogue no. SA00001-2, 1:10,000; anti-mouse, catalogue no. SA00001-1, 1:10,000; Proteintech, Rosemont, IL, USA) for 1 h at room temperature. Immunoreactive bands were visualized using enhanced chemiluminescence (ECL) detection reagents (catalogue no. RPN2232; Cytiva, Marlborough, MA, USA) and imaged with an Amersham Imager 680 system (Cytiva, Marlborough, MA, USA).

2.7 Data Collection and Expression Analysis

Microarray datasets related to liver fibrosis, including GSE1843, GSE103580, GSE49541, and GSE84044, were downloaded from the Gene Expression Omnibus (GEO) database (https://www.ncbi.nlm.nih.gov/geo/). *SEMA3C* expression levels were extracted to evaluate differential expression between normal and fibrotic tissues, across the three histological categories represented in GSE103580 (alcoholic steatosis, mild acute alcoholic hepatitis and alcoholic cirrhosis), and between mild and advanced fibrosis. Additionally, the correlation between *SEMA3C* expression and fibrosis grading and staging was assessed. For pan-cancer analysis, RNA sequencing data (in TPM format) and corresponding clinical phenotype data were obtained from The Cancer Genome Atlas (TCGA) database via the UCSC Xena platform (https://xena.ucsc.edu). After $\log_2$(TPM+1) transformation, differences in *SEMA3C* expression between unpaired tumor and normal samples, as well as paired tumor and adjacent non-tumor tissues (after $\log_2$FPKM+1 transformation), were compared using the Wilcoxon rank-sum test and Wilcoxon signed-rank test, respectively. Expression dynamics across different pathological stages were also analyzed using the one-way ANOVA test. Pathological stages were taken directly from the TCGA clinical annotation; tumours recorded as stage X (stage not assessable or not documented) were retained as a separate group. The number of samples analyzed for each cancer type is provided in **Supplementary Table 2**.

2.8 Stromal Marker Correlation and CAF Infiltration Analysis

Based on the TCGA pan-cancer expression matrix, Spearman correlations between *SEMA3C* expression and classic stromal, ECM, and epithelial-mesenchymal transition (EMT) marker genes (including *ACTA2*, *MMP3*, *MMP9*, *MMP14*, *FN1*, *FAP*, *PDGFRA*, *PDGFRB*, and *TGFB1*) were assessed using R software (Version 4.2.0, R Foundation for Statistical Computing, Vienna, Austria). Co-expression heatmaps were constructed following Z-score normalization of expression values. To evaluate the relationship between SEMA3C expression and the infiltration abundance of CAFs within the TME, four independent immune infiltration estimation algorithms were employed: EPIC, MCPCOUNTER, XCELL, and TIDE. Briefly, EPIC estimates the proportions of cancer cells, cancer-associated fibroblasts, endothelial cells and infiltrating immune subsets by constrained least-squares deconvolution of reference expression profiles; MCPCOUNTER scores the relative abundance of stromal and immune populations from the geometric mean of lineage-specific marker genes; XCELL converts cell-type-specific gene signatures into enrichment scores by single-sample gene set enrichment analysis (ssGSEA); and TIDE (Tumor Immune Dysfunction and Exclusion) quantifies microenvironmental components, including CAFs, within a framework designed to model tumor immune evasion. Partial Spearman correlation coefficients between *SEMA3C* expression and estimated CAF abundance were calculated with correction for tumor purity, using the TIMER2.0 web server (http://timer.cistrome.org). Results were visualized using the R package "ggplot2". No additional adjustment for multiple comparisons was performed on the *p* values obtained from the TIMER2.0 platform, and these results were therefore interpreted as exploratory. To mitigate the known limitations of transcriptomic deconvolution algorithms, including background predictions, multicollinearity, and reference dependency, the consistency of the associations was cross-validated across the four independent algorithms.

2.9 Prognostic and Diagnostic Value Assessment

Survival curves were generated with the Kaplan-Meier Plotter web portal (https://kmplot.com/analysis/) to assess the prognostic value of SEMA3C expression for OS across diverse malignancies. For every cohort, patients were dichotomized into high- and low-expression groups at the cut-off automatically selected by the platform (the "auto select best cutoff" option, which returns the expression threshold yielding the maximal separation between the two survival curves); the same procedure was applied uniformly to all eight cancer types, and no fixed median cut-off was imposed. Statistical significance was evaluated with the log-rank test, while hazard ratios (HR) with 95% confidence intervals (CI) were derived from univariate Cox proportional hazards regression. Additionally, receiver operat-

ing characteristic (ROC) curves were constructed using the "pROC" R package to evaluate the diagnostic efficacy of *SEMA3C* in distinguishing tumor tissues from normal tissues. The area under the curve (AUC) and its 95% CI were calculated.

2.10 Genetic Alteration and DNA Methylation Analysis

The cBioPortal for Cancer Genomics (https://www.cbioportal.org) was used to analyze the frequency of genetic alterations in *SEMA3C*, including mutations, amplifications, and deep deletions, across available TCGA cancer cohorts. Sample distributions were visualized using OncoPrint views, and mutation sites within the Sema and I-set protein domains were mapped using lollipop plots. The correlation between CNVstatus and *SEMA3C* mRNA expression levels was examined using Spearman correlation analysis. Furthermore, promoter methylation levels (Beta values) of *SEMA3C* were compared between primary tumor tissues and normal control tissues across multiple TCGA cancer types using the UALCAN portal (https://ualcan.path.uab.edu). Statistical testing was not performed for the promoter methylation comparison, and the beta value distributions are presented descriptively.

2.11 Functional and Gene Set Enrichment Analysis

Gene sets significantly correlated with *SEMA3C* were identified using R software. Functional enrichment analysis, including GO terms (Biological Process [BP], Cellular Component [CC], and Molecular Function [MF]) and Kyoto Encyclopedia of Genes and Genomes (KEGG) pathways, was performed using the "clusterProfiler" R package (version 4.4.4; Bioconductor). A false discovery rate (FDR) <0.05 was considered statistically significant. Further Gene Set Enrichment Analysis (GSEA) was conducted using GSEA software (Version 4.3.2, Broad Institute, Cambridge, MA, USA) against the MSigDB Hallmark gene sets, as well as KEGG, Reactome, and PID signaling pathways. Significance was determined based on normalized enrichment scores (NES), adjusted *p*-values (*p*.adj), and FDR. Gene sets with an FDR <0.05 were considered significantly enriched.

2.12 Statistical Analysis

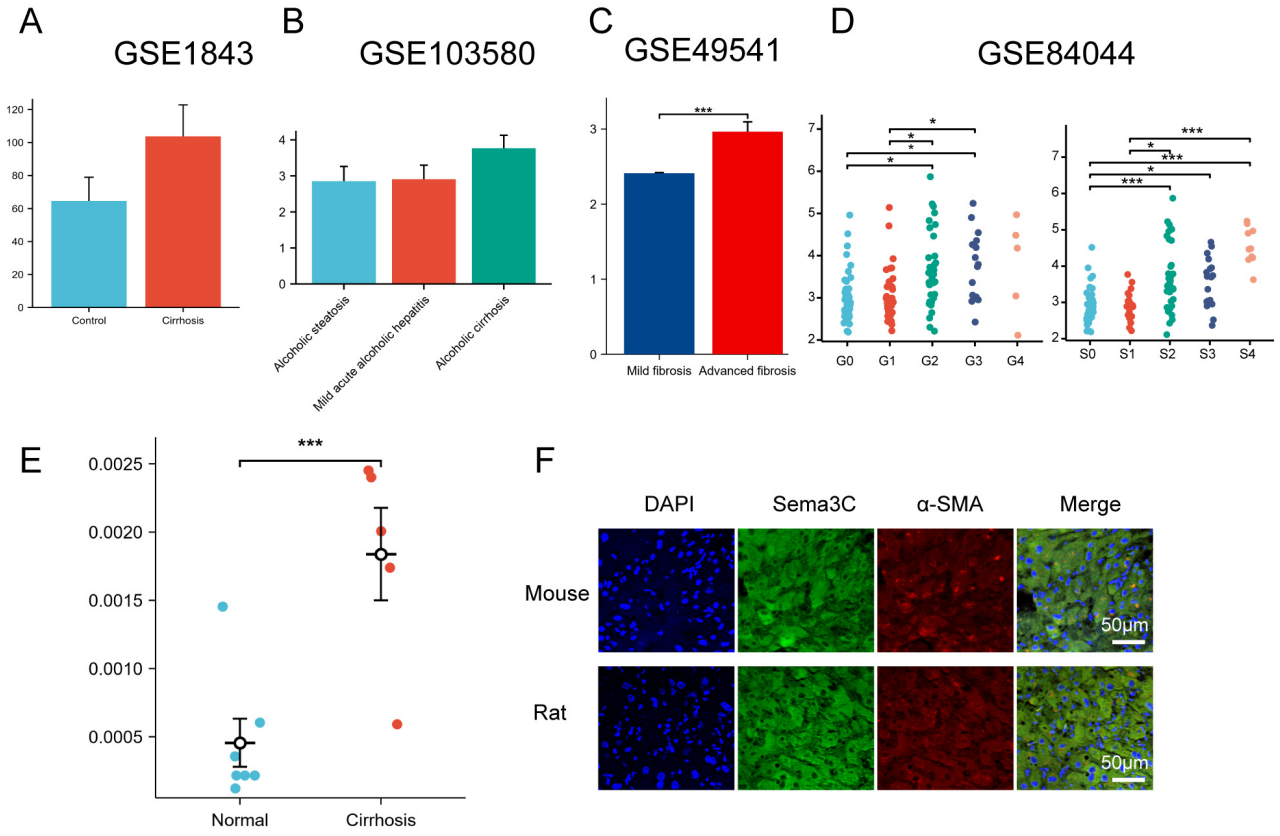
Data analysis and plotting were performed using R software (version 4.2.0, R Foundation for Statistical Computing, Vienna, Austria) and GraphPad Prism (version 9.5.0; GraphPad Software, San Diego, CA, USA). Normality was assessed using the Shapiro-Wilk test, and nonparametric tests were used where the assumption of normality was not met. Continuous variables were compared by Student's *t*-test or Wilcoxon rank-sum test, while multigroup differences were assessed by one-way ANOVA. Linear correlations were evaluated by Spearman correlation analysis. Survival outcomes were analyzed by the log-rank test, and diagnostic performance was determined by ROC curves. For analyses involving multiple comparisons across cancer types or algorithms, *p* values were adjusted using the Benjamini–Hochberg FDR method, except for those obtained directly from the TIMER2.0 platform, which were not additionally adjusted and were interpreted as exploratory (see section 2.8). A p-value < 0.05 was considered statistically significant.

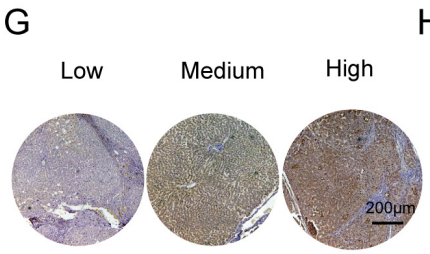
3. Results

3.1 SEMA3C Is Significantly Upregulated in Liver Fibrosis and Correlates With Pathological Progression

We first analyzed *SEMA3C* expression patterns across multiple public datasets from the GEO database. In the GSE1843 dataset, *SEMA3C* mRNA levels were higher in liver fibrosis tissues than in normal liver tissues (Fig. 1A). We next evaluated whether *SEMA3C* expression varies across different pathological stages. Analysis of the GSE103580 dataset, which comprises samples of alcoholic steatosis, mild acute alcoholic hepatitis and alcoholic cirrhosis, showed higher *SEMA3C* expression in alcoholic cirrhosis than in mild acute alcoholic hepatitis (Fig. 1B). Similarly, a comparison within the GSE49541 dataset revealed elevated *SEMA3C* levels in advanced fibrosis stages compared with mild stages (Fig. 1C). Consistent with these trends, data from the GSE84044 dataset demonstrated that *SEMA3C* expression positively correlated with both the pathological grade and stage of liver fibrosis (Fig. 1D). Collectively, these multi-cohort bioinformatic data indicate that *SEMA3C* is upregulated in fibrotic livers in a severity-dependent manner.

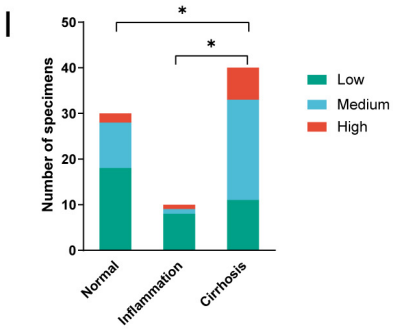
These bioinformatic findings were subsequently validated using clinical specimens and animal models. Quantitative PCR (qPCR) analysis confirmed that *SEMA3C* mRNA expression was significantly higher in clinical liver fibrosis samples than in normal controls (Fig. 1E). This upregulation was further supported at the protein level by TMA analysis, which showed that *SEMA3C* protein expression was markedly increased in liver fibrosis tissues compared to both normal liver and chronic hepatitis tissues (Fig. 1G–I). We next performed immunofluorescence co-localization staining to identify the specific cell types expressing *SEMA3C* in the fibrotic microenvironment. The results demonstrated that *SEMA3C* prominently co-localized with classic markers of activated HSCs in mouse and rat liver fibrosis models (Fig. 1F). Furthermore, co-expression analysis in hepatocellular carcinoma tissues revealed a strong positive correlation between *SEMA3C* expression and classic fibrosis-related genes (Fig. 1J). Taken together, these data indicate that *SEMA3C* is upregulated in fibrotic liver tissue in both human and rodent samples, and that in the mouse and rat models examined it co-localizes predominantly with activated HSCs. Because cell-type-specific localization could not be assessed in human tissue in the present study, the human data describe tissue-level expression rather than a defined cellular source.

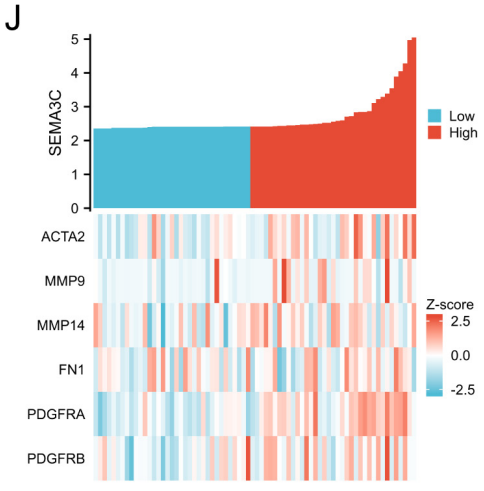


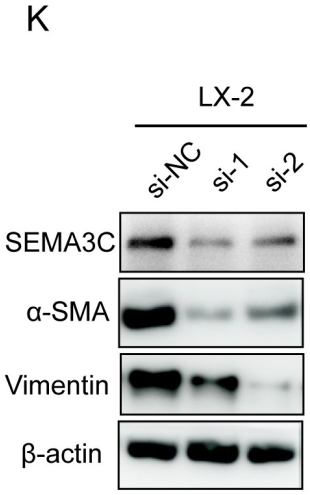


H

	Score			
	Low	Medium	High	Total
Normal	18	10	2	30
Inflammation	8	1	1	10
Cirrhosis	11	22	7	40







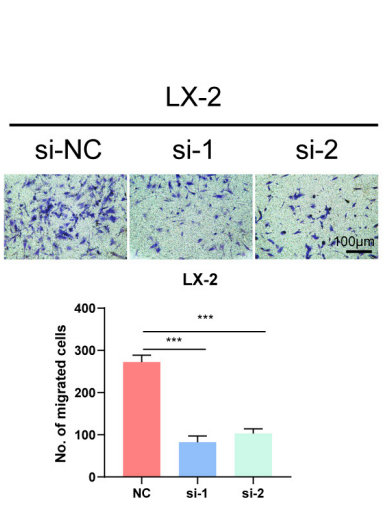


Fig. 1. Semaphorin 3C (*SEMA3C*) is upregulated in liver fibrosis and correlates with pathological severity. (A) Differential expression of *SEMA3C* between normal and fibrotic liver tissues in the GSE1843 dataset. (B) Comparison of *SEMA3C* transcriptional levels between alcoholic steatosis, mild acute alcoholic hepatitis, and alcoholic cirrhosis in the GSE103580 dataset. (C) Relative *SEMA3C* mRNA levels in mild versus advanced fibrosis in the GSE49541 cohort. (D) Spearman correlation analysis demonstrating the association of *SEMA3C* expression with pathological grading and staging of liver fibrosis in the GSE84044 dataset. (E) Quantitative real-time PCR (qPCR) validation of *SEMA3C* mRNA expression in clinical human liver fibrosis samples (n = 5) and normal liver control tissues (n = 7). Each specimen was measured in technical triplicate and averaged to one value per specimen; bars show mean ± SD across individual specimens, reflecting biological variation between patients. (F) Representative immunofluorescence co-localization staining images showing the cellular distribution of *SEMA3C* (green) and the α-SMA (red) in mouse and rat liver fibrosis models (Scale bars, 50 μm). Nuclei were counterstained with DAPI (blue). (G) Representative IHC images illustrating *SEMA3C* staining intensity across normal liver (n = 30), inflammation (n = 10), and liver fibrosis (n = 40) tissues (Scale bar, 200 μm). (H) Statistical analysis of *SEMA3C* immunoreactivity scores in the normal liver (n = 30), inflammation (n = 10), and liver fibrosis (n = 40) groups. (I) Distribution of the three immunoreactivity categories among the three groups. (J) Heatmap illustrating the expression profiles of classical fibrosis-related marker genes stratified by *SEMA3C* expression levels in liver hepatocellular carcinoma (LIHC) tissues. (K) WB confirmation of *SEMA3C* knockdown efficiency alongside alterations in fibrotic markers (α-SMA, Vimentin) in LX-2. (L) Transwell migration assays in LX-2 cells transfected with control siRNA (si-NC) or *SEMA3C*-specific siRNAs (si-*SEMA3C*-1, si-*SEMA3C*-2), Scale bar: 100 μm. Statistical analysis. (A,C) Two-sided Wilcoxon rank-sum test. (B) Kruskal–Wallis test followed by Dunn's multiple comparison test. (D) Spearman's rank correlation, with r encoded by colour and *p* values given in the panels. (E) Two-sided Wilcoxon rank-sum test; each specimen was measured in technical triplicate and averaged to one value, and bars show mean ± SD across the individual specimens (n = 7 normal, n = 5 fibrotic). (F,G) Representative images. (H) Numbers of specimens in each immunoreactivity category. (I) Categories scored as ordinal ranks (low = 1, medium = 2, high = 3) and compared across the three groups by the Kruskal–Wallis test ($p = 0.0017$), followed by Dunn's multiple comparison test; the bracket indicates inflammation versus cirrhosis. (K) Representative western blots of SEMA3C and fibrotic markers in LX-2 cells transfected with si-NC, si-*SEMA3C*-1 or si-*SEMA3C*-2. (L) One-way ANOVA followed by Dunnett's test versus si-NC; bars show mean ± SD of three independent biological replicates. $*p < 0.05$, $***p < 0.001$ by Student's *t*-test, Wilcoxon rank-sum test, or Kruskal-Wallis test where appropriate.

The functional role of *SEMA3C* in HSC activation and behavior was further investigated through knockdown experiments in the human HSC cell line, LX-2. The representative western blotting images showed reduced protein levels of SEMA3C and α-SMA in LX-2 cells transfected with SEMA3C-specific siRNAs, particularly with si-*SEMA3C*-1 or si-*SEMA3C*-2, while changes in vimentin varied between the two siRNAs (Fig. 1K). Moreover, functional assays demonstrated that knockdown with either siRNA suppressed the migratory capacity of LX-2 cells (Fig. 1L). Taken together, these *in vitro* data support a role for *SEMA3C* in promoting the phenotypic activation and migration of HSCs, thereby contributing to the progression of liver fibrosis.

3.2 SEMA3C Is Widely Overexpressed in Multiple Malignancies and Correlates With Advanced Pathological Stages

We expanded our investigation to a pan-cancer scale to characterize the transcriptional profile of *SEMA3C* across diverse human malignancies using TCGA cohorts. Initial evaluation of unpaired samples demonstrated that *SEMA3C* expression was significantly elevated in tumor tissues compared with normal tissues across a wide range of cancer types (Fig. 2A). To minimize the potential confounding effects of individual genetic backgrounds, we subsequently performed a paired analysis using matched tumor and adjacent para-tumor tissues. *SEMA3C* mRNA levels remained consistently higher in the malignant tissues than in their corresponding normal counterparts across multiple cancer types (Fig. 2B).

We next evaluated the clinical relevance of this overexpression by analyzing the relationship between *SEMA3C* levels and tumor progression. *SEMA3C* expression exhibited a significant positive correlation with individual pathological stages across various malignant tumors, with higher expression observed in advanced stages (Fig. 2C). Taken together, these pan-cancer data demonstrate that *SEMA3C* is widely overexpressed in human cancers and closely associates with clinical disease progression.

3.3 SEMA3C Expression Positively Correlates With Stromal Marker Genes and Cancer-Associated Fibroblast Infiltration in Pan-Cancer Cohorts

Given that *SEMA3C* co-localized predominantly with activated HSCs in the fibrotic liver (Fig. 1F), we investigated whether *SEMA3C* is broadly associated with stromal activation and ECM remodeling in other malignancies. We evaluated the co-expression relationship between SEMA3C and a panel of classic stromal and EMT markers, including *ACTA2*, *FAP*, *FN1*, *TGFB1*, and *MMP*s. Patients from eight selected TCGA cancer cohorts were grouped

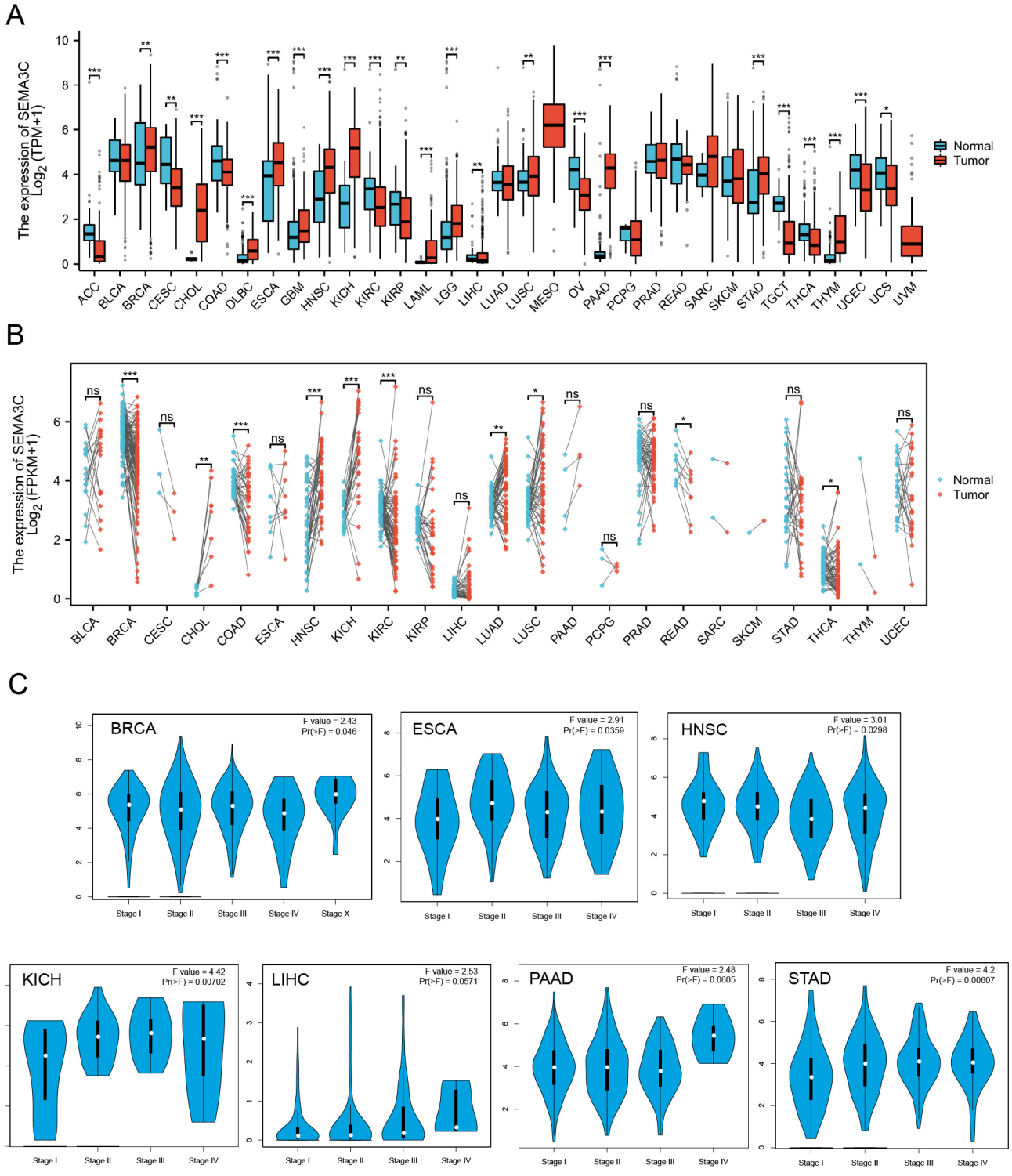


Fig. 2. *SEMA3C* is widely overexpressed across multiple cancers and correlates with advanced pathological stages. (A) Pan-cancer transcriptomic profile of *SEMA3C* mRNA expression in unpaired primary tumor tissues (n = 10,157) and normal control samples (n = 740) across the TCGA cohorts analyzed; the number of samples in each cancer type is provided in **Supplementary Table 2**. (B) Paired comparison of *SEMA3C* transcriptional levels between matched tumor and adjacent para-tumor tissues from identical patients (n = 2316 paired cases; per-cancer numbers are provided in **Supplementary Table 2**). (C) Expression levels of *SEMA3C* in distinct pathological stages (Stages I, II, III, IV, and X) in multiple human malignant tumors; the BRCA panel additionally includes a Stage X group, i.e., tumours with no documented pathological stage. the number of samples in each stage group is provided in **Supplementary Table 2**. Statistical significance was determined by the Wilcoxon rank-sum test for unpaired samples, the Wilcoxon signed-rank test for paired cohorts, and one-way ANOVA for multi-group clinical stage comparisons. *$p < 0.05$, **$p < 0.01$, ***$p < 0.001$; ns, not significant.

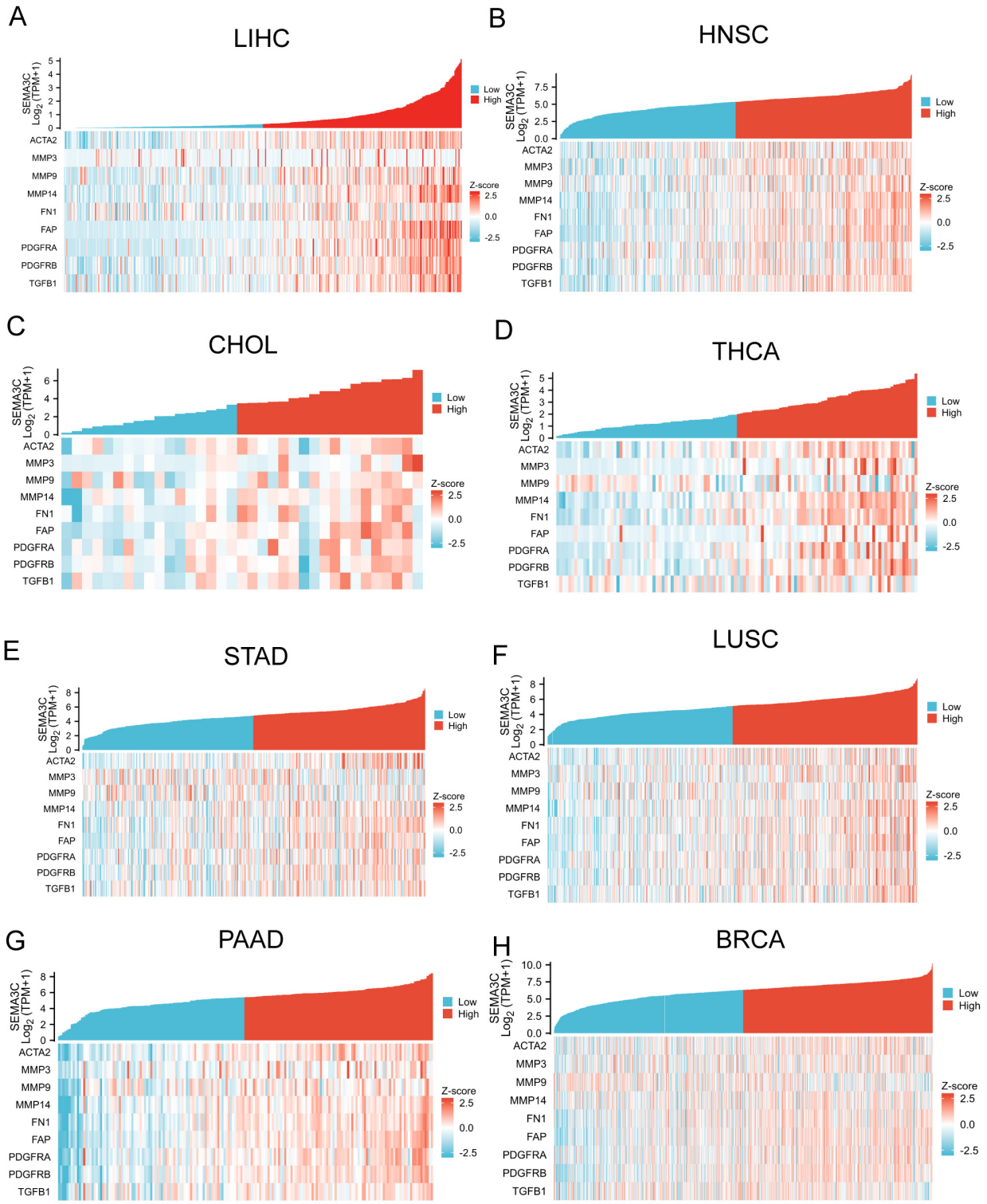


Fig. 3. *SEMA3C* expression positively correlates with canonical stromal markers across diverse malignant tumors. Co-expression heatmaps demonstrated the transcriptional correlation between *SEMA3C* and a panel of classical stromal, ECM, and EMT marker genes (including *ACTA2*, *MMP3*, *MMP9*, *MMP14*, *FN1*, *FAP*, *PDGFRA*, *PDGFRB*, and *TGFB1*) across eight selected tumors. Patients within each cohort were divided into SEMA3C-high and SEMA3C-low groups based on the median expression cut-off. Synchronized upregulation of the stromal signatures is displayed for (A) LIHC, (B) head and neck squamous cell carcinoma (HNSC), (C) cholangiocarcinoma (CHOL), (D) thyroid Carcinoma (THCA), (E) stomach adenocarcinoma (STAD), (F) lung squamous cell carcinoma (LUSC), (G) pancreatic adenocarcinoma (PAAD), and (H) breast invasive carcinoma (BRCA). Expression values within the heatmaps are displayed following Z-score normalization.

into *SEMA3C*-high and *SEMA3C*-low categories based on the expression levels. High *SEMA3C* expression was accompanied by a coordinated upregulation of these stromal markers across multiple tumor types. This synchronized expression pattern was highly pronounced in liver hepatocellular carcinoma (LIHC) (Fig. 3A), HNSC (Fig. 3B), CHOL (Fig. 3C), THCA (Fig. 3D), and stomach adenocarcinoma (STAD) (Fig. 3E), and consistently persisted in lung squamous cell carcinoma (LUSC), pancreatic adenocarcinoma (PAAD), and breast invasive carcinoma (BRCA) cohorts (Fig. 3F–H). These findings highlight a generalized association between *SEMA3C* and stromal reactivation in human cancers, indicating a robust transcriptional link between *SEMA3C* and stromal matrix reactivation across diverse cancer types.

To identify the specific cellular component corresponding to this stromal signature, we evaluated the relationship between *SEMA3C* expression and the infiltration abundance of CAFs within the TME. We utilized four independent quantification algorithms—EPIC, MCPCOUNTER, XCELL, and TIDE—to estimate CAF infiltration levels. *SEMA3C* expression demonstrated widespread positive correlations with estimated CAF abundance across the majority of TCGA cohorts (Fig. 4). Notably, this association was highly consistent and statistically significant ($p < 0.05$) across all four algorithms in malignancies that heavily rely on a microenvironmental stroma, including LIHC, STAD, HNSC, and THCA (Fig. 4). Non-significant associations ($p > 0.05$) were rare and limited to a few specific tumor types, such as KICH and UVM (Fig. 4). Combined with the co-expression profiles of marker genes, these microenvironmental data suggest that *SEMA3C* expression is closely linked to the presence and activation of CAFs within the tumor stroma.

3.4 Prognostic Significance and Diagnostic Value of SEMA3C Expression Across Multiple Human Cancers

To evaluate the clinical relevance of *SEMA3C* in patients with malignancies, we performed Kaplan-Meier survival analysis to determine the association between its expression levels and long-term prognosis. High *SEMA3C* expression was significantly correlated with shortened OS across eight distinct TCGA cohorts. Specifically, elevated *SEMA3C* levels predicted poor survival outcomes in cervical squamous cell carcinoma (CESC; HR = 2.52, $p = 0.0026$) (Fig. 5A), head and neck squamous cell carcinoma (HNSC; HR = 1.66, $p = 0.00019$) (Fig. 5B), kidney renal clear cell carcinoma (KIRC; HR = 1.60, $p = 0.0025$) (Fig. 5C), and kidney renal papillary cell carcinoma (KIRP; HR = 2.58, $p = 0.0017$) (Fig. 5D). This unfavorable prognostic association was also confirmed in hepatocellular carcinoma (LIHC; HR = 1.55, $p = 0.012$) (Fig. 5E), lung adenocarcinoma (LUAD; HR = 1.64, $p = 0.0017$) (Fig. 5F), stomach adenocarcinoma (STAD; HR = 1.48, $p = 0.021$) (Fig. 5G), and thyroid carcinoma (THCA; HR = 3.32, $p = 0.014$) (Fig.

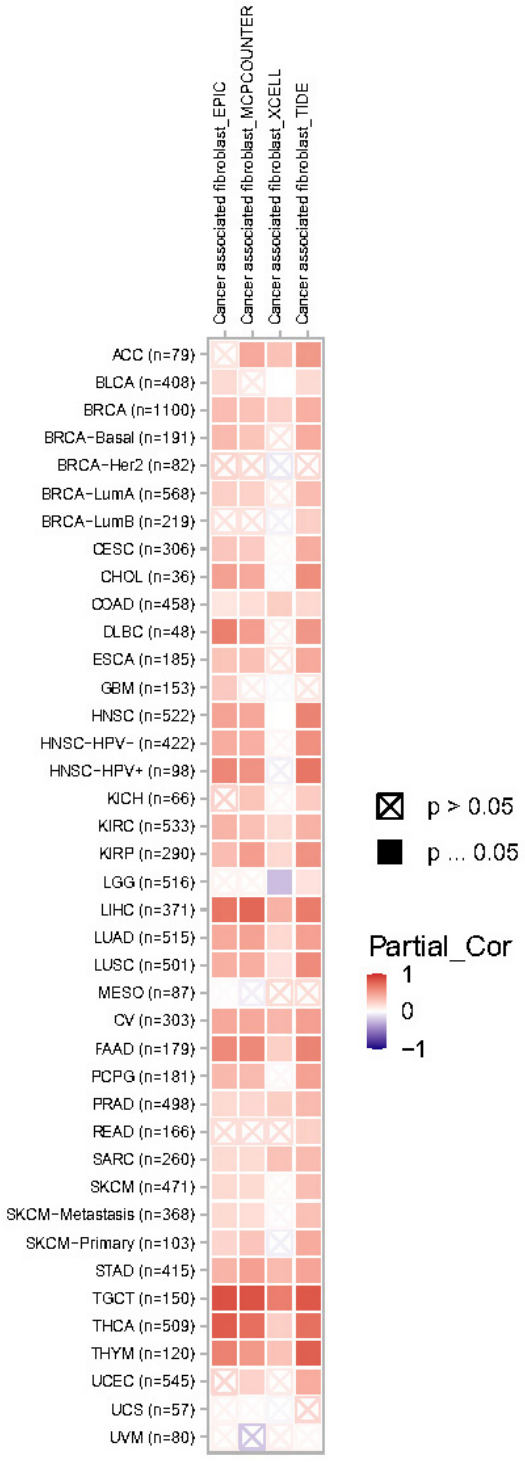


Fig. 4. *SEMA3C* expression positively correlates with the infiltration abundance of CAFs across the pan-cancer spectrum. Pan-cancer correlation profiles demonstrated the relationship between *SEMA3C* mRNA expression levels and estimated CAF infiltration abundance across diverse TCGA cohorts utilizing four independent computational algorithms: EPIC, MCPCOUNTER, XCELL, and TIDE. The number of tumor samples analyzed for each cancer type is provided in **Supplementary Table 2**.

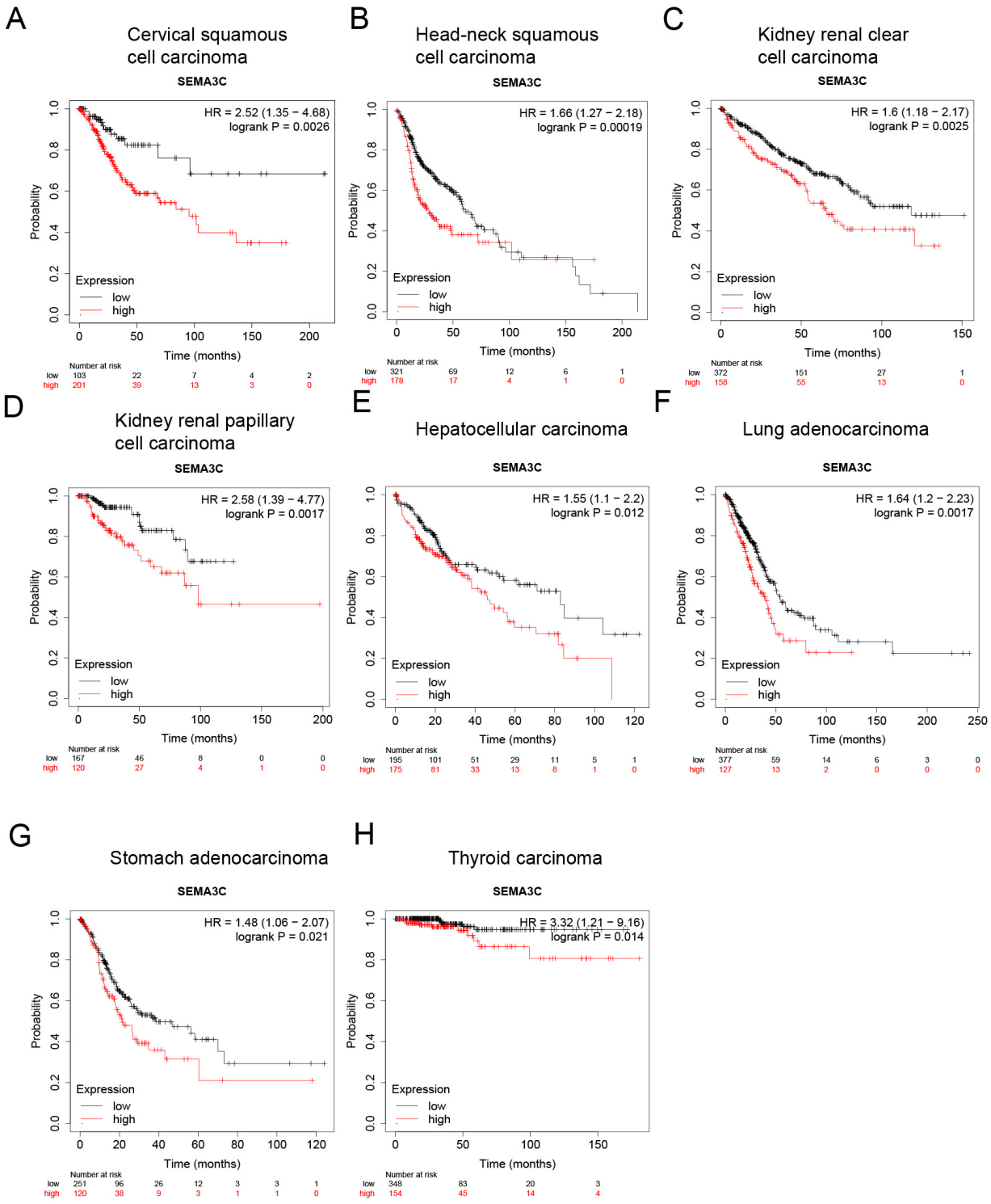


Fig. 5. Prognostic significance of elevated *SEMA3C* expression across several cancers. Kaplan-Meier survival curves indicated the association between *SEMA3C* mRNA expression levels and OS across eight cancer types: (A) cervical squamous cell carcinoma; (B) head and neck squamous cell carcinoma; (C) kidney renal clear cell carcinoma; (D) kidney renal papillary cell carcinoma; (E) hepatocellular carcinoma; (F) lung adenocarcinoma; (G) stomach adenocarcinoma and (H) thyroid carcinoma. Patients within each malignant cohort were separated into high- and low-expression groups at the cut-off automatically selected by the Kaplan-Meier Plotter (best separation between the two curves); because the cut-off is data-driven, the two groups differ in size within each cohort, and the numbers of patients at risk are given beneath each panel. Statistical significance between the high- and low-expression curves was evaluated via the log-rank test.

5H). These results indicate that SEMA3C expression is a shared indicator of poor prognosis in various cancer types.

Next, ROC curves were constructed to assess the efficacy of *SEMA3C* mRNA levels in distinguishing malignant tissues from normal controls. *SEMA3C* demonstrated stable diagnostic performance across a pan-cancer spectrum (Fig. 6). In breast invasive carcinoma (BRCA), the area under the curve (AUC) was 0.777 (Fig. 6A), while it reached 0.836 in CESC (Fig. 6B). Notably, *SEMA3C* exhibited the highest diagnostic accuracy in cholangiocarcinoma (CHOL), with an AUC value of 0.946 (Fig. 6C). Reliable diagnostic capacity was also verified in glioblastoma multiforme (GBM; AUC = 0.817) (Fig. 6D), HNSC (AUC = 0.749) (Fig. 6E), KIRC (AUC = 0.708) (Fig. 6F), oral squamous cell carcinoma (OSCC; AUC = 0.766) (Fig. 6G), prostate adenocarcinoma (PRAD; AUC = 0.714) (Fig. 6H), and uterine corpus endometrial carcinoma (UCEC; AUC = 0.701) (Fig. 6I). Collectively, these findings show that *SEMA3C* possesses substantial value as both a prognostic and diagnostic biomarker in various malignant tumors.

3.5 Genomic Amplification and Promoter Hypomethylation Are Associated With SEMA3C Overexpression in Human Cancers

To elucidate the upstream mechanisms driving the widespread upregulation of *SEMA3C* in human malignancies, we investigated its genetic and epigenetic alteration profiles using the cBioPortal and TCGA databases.

We first assessed the genetic variation of *SEMA3C* across multiple cancer cohorts. The alteration frequency analysis revealed that gene amplification was the predominant type of genetic alteration across most cancer types, followed by mutations (Fig. 7A). The detailed distribution of these genomic changes among individual tumor samples was visualized using an OncoPrint summary (Fig. 7B). Furthermore, mutation mapping showed that genetic alterations were scattered across the entire *SEMA3C* sequence, with a considerable portion located within the functional Sema and I-set domains (Fig. 7C). To determine whether these structural changes affect transcriptional output, we evaluated the relationship between CNV status and mRNA levels. The results demonstrated a robust positive correlation, indicating that CNV gain and amplification are associated with elevated *SEMA3C* expression (Fig. 7D).

Beyond genetic modifications, epigenetic regulation, such as DNA methylation, plays a critical role in gene transcription. Therefore, we compared the promoter methylation levels (Beta values) of *SEMA3C* between primary tumors and adjacent normal tissues. Across a wide spectrum of cancers—including BLCA, BRCA, COAD, CESC, ESCA, HNSC, KIRP, LIHC, LUSC, PAAD, PRAD, and STAD—*SEMA3C* promoter methylation was lower in tumor tissues than in normal controls (Fig. 7E).

Collectively, these data suggest that both genomic amplification and epigenetic promoter hypomethylation serve as key upstream events driving the aberrant overexpression of *SEMA3C* in the TME.

3.6 Downstream Functional Enrichment Links SEMA3C to ECM Remodeling and Classical Fibrogenic Pathways

To explore the downstream molecular mechanisms mediating the role of *SEMA3C* in stromal activation, we performed functional enrichment analysis on *SEMA3C*-related genes. GO analysis revealed that these genes were highly enriched in biological processes and cellular components primarily related to ECM organization, cell junction assembly, and collagen-containing ECM (Fig. 8A). Consistently, KEGG pathway analysis indicated significant involvement in ECM-receptor interaction, focal adhesion, and the Wnt signaling pathway (Fig. 8B).

To further validate these molecular shifts at the global transcriptomic level, we conducted GSEA comparing *SEMA3C*-high and *SEMA3C*-low expression groups. Analysis using the Hallmark gene sets demonstrated that elevated SEMA3C expression was strongly associated with the activation of epithelial-mesenchymal transition (EMT) and angiogenesis (Fig. 8C). Furthermore, cross-database GSEA utilizing KEGG, Reactome, and PID datasets indicated matrix remodeling and fibrogenesis pathways, specifically including ECM organization andcollagen degradation (Fig. 8D).

Taken together, these functional data support our earlier phenotypic observations, indicating that *SEMA3C* is closely associated with fibrotic progression and TME remodeling through extensive ECM reorganization and the activation of classical stromal signaling cascades.

4. Discussion

Tissue fibrosis and the TME share core pathological features, most notably the aberrant remodeling of the ECM driven by activated stromal cells [22,23]. This study identifies Semaphorin 3C (*SEMA3C*) as a conserved regulatory node across both conditions. Our data indicate that *SEMA3C* is expressed in activated HSCs and is associated with liver fibrogenesis, although direct *in vivo* evidence for a causal role is still lacking. Extending to a pan-cancer scale, SEMA3C is widely upregulated—driven by gene amplification and promoter hypomethylation—and tightly correlates with CAF infiltration and poor clinical outcomes.

We acknowledge that previous independent studies have reported *SEMA3C* enrichment in cirrhotic livers, its expression in HSCs, and its pro-fibrotic function mediated by NRP2. The present study extends these observations by systematically integrating cross-species experimental validation with pan-cancer multi-omics analyses, thereby positioning *SEMA3C* as a conserved stromal regulator at the fibro-cancerous interface and underscoring its translational value as a diagnostic and prognostic biomarker.

Although SEMA3C is canonically recognized as an axon guidance molecule, emerging evidence implicates it

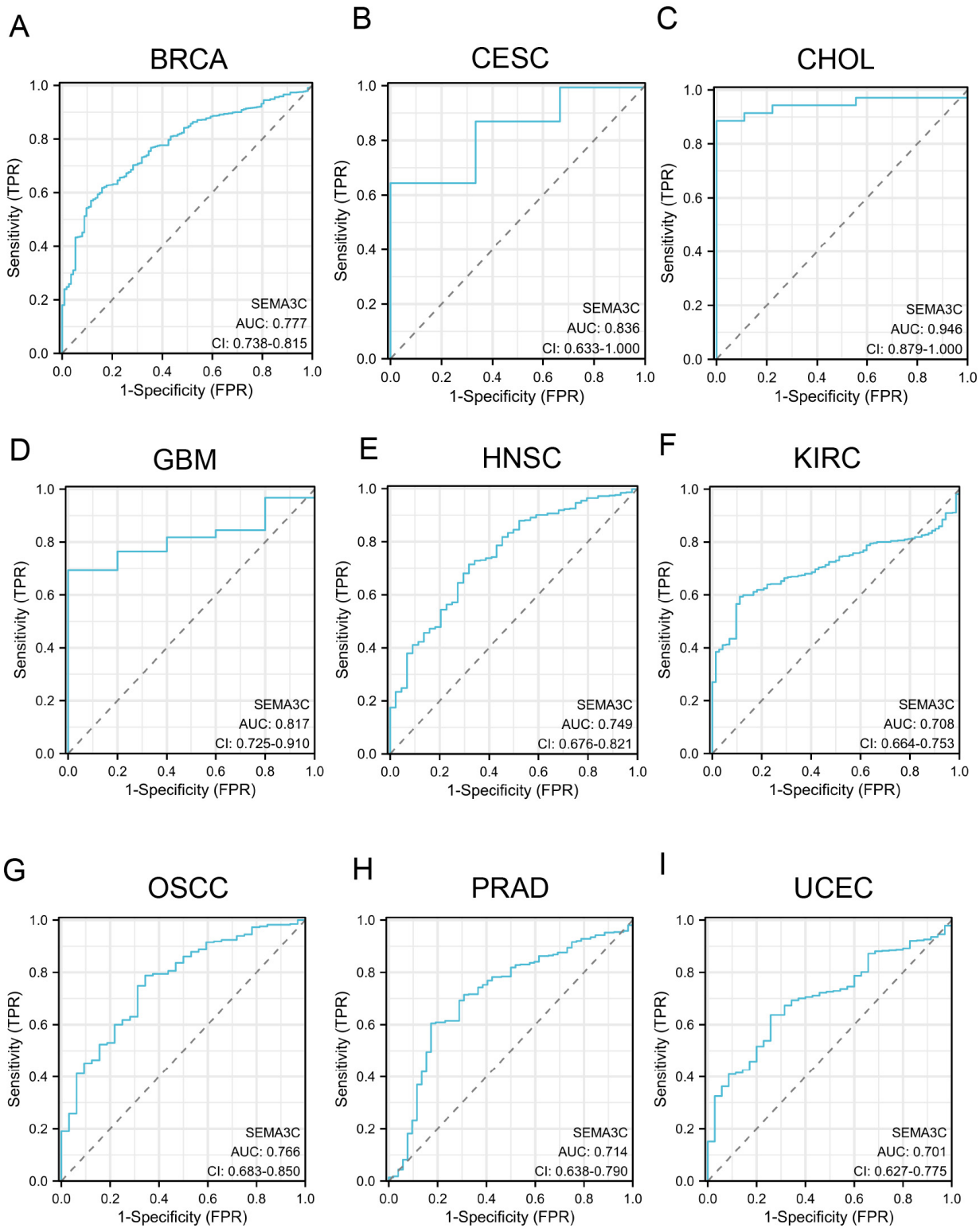


Fig. 6. Diagnostic efficacy of *SEMA3C* expression in different tumors from normal control tissues. ROC curves evaluating the diagnostic accuracy of *SEMA3C* mRNA expression levels across several cancers within the TCGA cohorts: (A) breast invasive carcinoma (BRCA), (B) cervical squamous cell carcinoma (CESC), (C) cholangiocarcinoma (CHOL), (D) glioblastoma multiforme (GBM), (E) head and neck squamous cell carcinoma (HNSC), (F) kidney renal clear cell carcinoma (KIRC), (G) oral squamous cell carcinoma (OSCC), (H) prostate adenocarcinoma (PRAD), and (I) uterine corpus endometrial carcinoma (UCEC). The diagnostic performance was quantified by the area under the curve (AUC) value alongside its 95% confidence interval (CI). A higher AUC value indicated a superior capacity of *SEMA3C* expression to differentiate malignant tissues from normal counterparts.

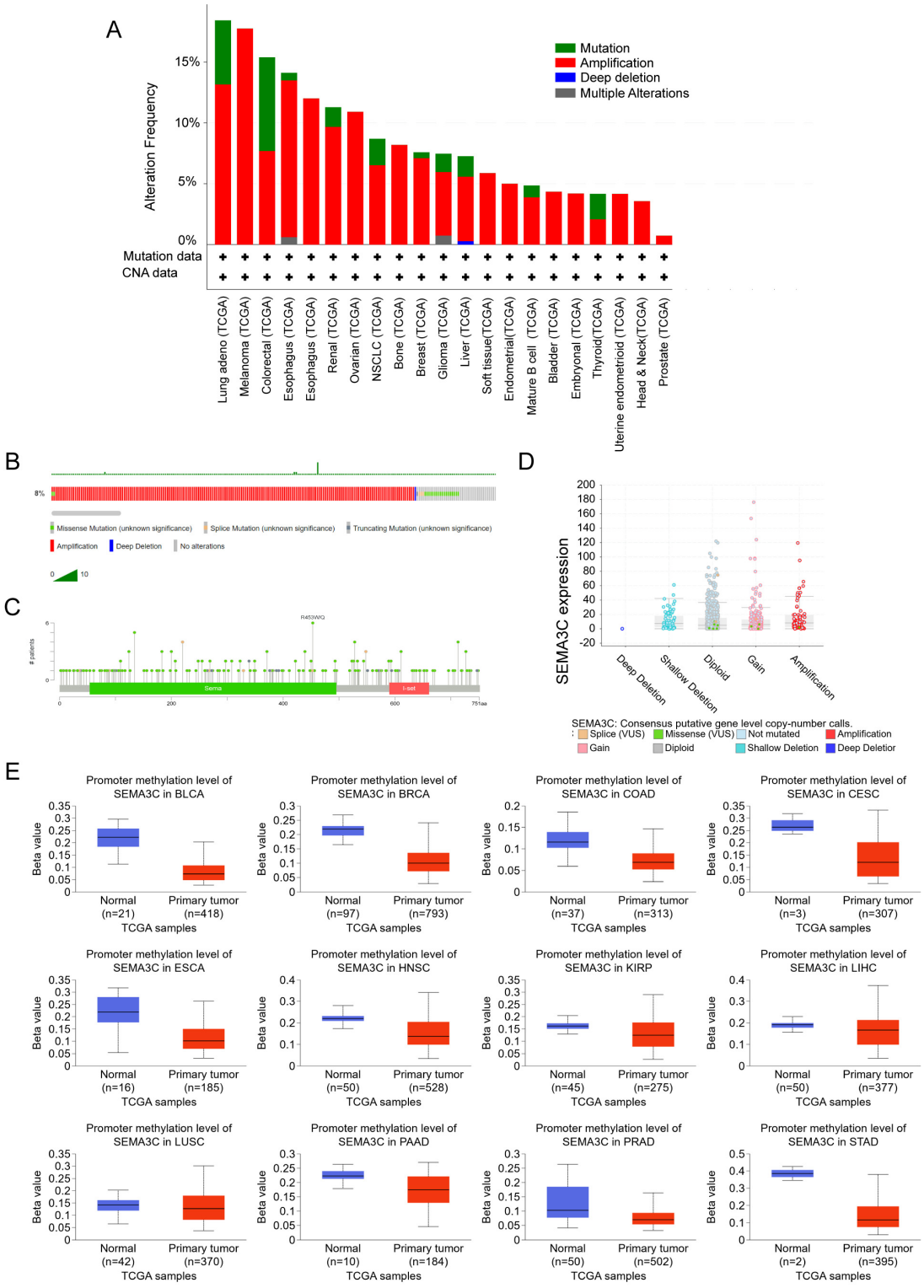


Fig. 7. Genomic amplification and promoter hypomethylation are associated with *SEMA3C* overexpression in human cancers. (A) Overview of genetic alteration frequencies, indicating that gene amplification is the predominant structural variant type. (B) OncoPrint matrix summary showed the detailed distribution and types of genomic alterations across individual tumor samples. (C) Lollipop mutation plot mapping specific genetic mutation sites across the functional Sema and I-set protein domains of *SEMA3C*. (D) Spearman correlation analysis evaluating the relationship between CNV status and corresponding *SEMA3C* mRNA expression levels. (E) Epigenetic promoter methylation analysis. Comparison of promoter methylation levels of *SEMA3C* between tumors and adjacent normal tissues across multi-cancer cohorts via the UALCAN portal.

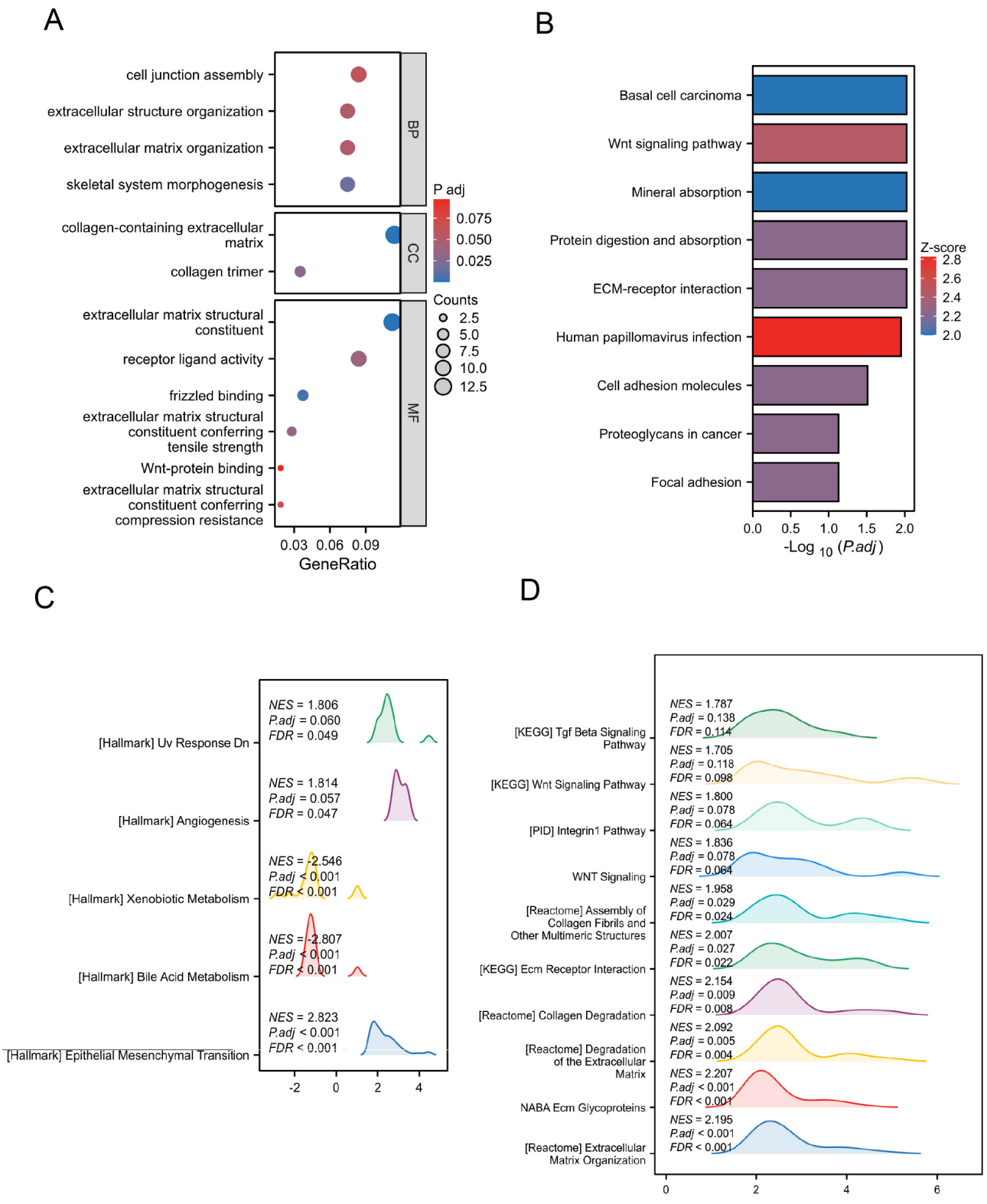


Fig. 8. Downstream functional enrichment of *SEMA3C* related pathways. (A) Gene Ontology (GO) plot showed enrichment in ECM organization and collagen networks. (B) Kyoto Encyclopedia of Genes and Genomes (KEGG) bar plot showing enrichment in ECM-receptor interaction, focal adhesion, and Wnt signaling. (C) GSEA demonstrated a positive correlation of high *SEMA3C* expression with EMT. (D) GSEA (KEGG, Reactome, and PID databases) showed transcriptomic enrichment in ECM associated pathways. Statistical significance was defined by a FDR <0.05. GSEA results are presented using Normalized Enrichment Scores (NES) and adjusted *p* values.

in tissue repair and tumor progression. Our experimental data support a pro-fibrotic role for *SEMA3C* in the liver. Both transcriptomic analysis and clinical tissue validation confirmed that *SEMA3*C is significantly upregulated in fibrotic livers, correlating with pathological severity. In mouse and rat liver fibrosis models, immunofluorescence localized *SEMA3C* primarily to activated HSCs rather than hepatocytes, indicating that *SEMA3C* behaves as a microenvironment-responsive factor in the fibrotic liver. *In vitro* knockdown in LX-2 cells attenuated cellular migration and the expression of classic fibrotic markers (e.g., *ACTA2*). Collectively, these results are consistent with a role for *SEMA3C* in HSC activation during liver fibrosis, whereas a causal requirement for *SEMA3C* in fibrogenesis *in vivo* remains to be established.

Building upon its pro-fibrotic role in the liver, we investigated whether *SEMA3C* functions as a universal stromal modulator in the pan-cancer microenvironment. Our analysis revealed a robust pan-cancer association between high *SEMA3C* expression and the enrichment of ECM organization and CAF infiltration. Specifically, *SEMA3C* expression showed significant positive correlations with canonical stromal markers, including *ACTA2*, *FAP*, and MMPs, across multiple TCGA cohorts. This systemic link implies that the oncogenic role of *SEMA3C* is intimately tied to shaping a reactive, pro-tumorigenic stromal compartment.

Notably, our pan-cancer analysis revealed that the correlation between *SEMA3C* expression and CAF infiltration is particularly pronounced in digestive system tumors, such as hepatocellular carcinoma (LIHC) and stomach adenocarcinoma (STAD), compared with certain non-digestive malignancies. This discrepancy may be attributed to the unique pathological microenvironment of the gastrointestinal tract and liver, where cancer development is frequently driven by a classic "inflammation-fibrosis-cancer" axis [24]. In these organs, chronic inflammatory injury heavily primes the stromal niche, leading to extensive ECM remodeling [25]. Consequently, pro-fibrotic factors like *SEMA3C* may be more dynamically engaged in maintaining this activated stromal state in digestive cancers than in tumors arising from less fibrogenic backgrounds.

To elucidate the upstream drivers of *SEMA3C* dysregulation, we analyzed its genetic and epigenetic landscape. SEMA3C is pervasively upregulated across cancer types, consistent with its established oncogenic role in multiple malignancies [26]. The hypomethylation status further suggests that its transcriptional activation is highly responsive to environmental stress. Downstream, functional enrichment analyses linked *SEMA3C* to the TGF-β and Wntsignaling pathways, as well as integrin interactions [27]. While neuropilins and plexins are standard class 3 semaphorin receptors, receptor crosstalk with integrins or TGF-β signaling frequently coordinates ECM remodeling [28]. Our GSEA results are consistent with this receptor crosstalk model; however, direct receptor-binding and downstream signaling experiments are required to definitively establish the receptor complexes through which *SEMA3C* mediates stromal remodeling.

Beyond these cell-intrinsic receptor events, *SEMA3C* is likely to operate within a broader, self-reinforcing hepatosplenic circuit that links intrahepatic fibrogenesis to systemic inflammation [29]. In the injured liver, *SEMA3C* engages NRP2, the neuropilin receptor that is preserved during HSC transdifferentiation, and enhances SMAD2/3 responsiveness, thereby sensitizing HSCs to canonical TGF-β1 signaling [30]. This engagement also recruits the class 3 semaphorin signaling machinery, which couples neuropilin/plexin activation to Rho GTPase-dependent cytoskeletal remodeling [16] and to integrin-linked FAK signaling [28]. SEMA3C further reinforces NF-κB activation and the release of IL-6 [27] and promotes the intrahepatic recruitment of splenic leukocytes, a process in which spleen-derived monocytes and macrophages have been shown to migrate into the fibrotic liver and to activate HSCs [31]. Conversely, the accompanying increase in ECM stiffness and actomyosin contractility raises sinusoidal resistance and contributes to portal hypertension, promoting splenic congestion and the spillover of spleen-derived inflammatory mediators, including TNF, back to the liver through the portal circulation [32]. In parallel, *SEMA3C*-driven enhancement of cholesterol biosynthesis and metabolic reprogramming stabilizes the myofibroblast phenotype and sustains collagen I/III deposition [27]. Together, these events constitute a closed-loop amplifier in which splenic inflammatory output activates HSCs, *SEMA3C* heightens HSC sensitivity to these cues, and activated HSCs in turn release additional inflammatory mediators that further stimulate splenic immune niches [31].

Viewed in this way, *SEMA3C* emerges as a TGF-β-sensitizing, NRP2-dependent molecular hub that integrates mechanical stress, cytokine signaling and immune-cell trafficking, and that thereby tightens the bidirectional communication of the liver–spleen axis. Because activated HSCs and CAFs share a common myofibroblastic program, an analogous circuit may also operate at the fibrocancerous interface, where a sustained stromal *SEMA3C* pool could couple the local desmoplastic reaction to the systemic inflammatory tone that favors tumor progression. It should be emphasized, however, that these signaling events are assembled from the studies cited above rather than demonstrated in the present work; HSC-specific or NRP2 loss-of-function models, portal–systemic cytokine gradient measurements, and spleen-targeted interventions such as splenectomy or spleen-directed delivery will be required to determine whether *SEMA3C* is causally embedded in this axis.

The translational potential of *SEMA3C* is underscored by its significant prognostic and diagnostic value. Kaplan-Meier analyses identified high *SEMA3C* expression as a

consistent predictor of poor OS across multiple independent cancer cohorts. At the same time, ROC curve analysis demonstrated its robust diagnostic accuracy, particularly in stroma-rich cancers such as cholangiocarcinoma (CHOL). These clinical utilities reinforce its role as an indicator of aggressive disease. Future therapeutic strategies could potentially target *SEMA3C* or the downstream signaling to intercept the desmoplastic reaction and disrupt the fibro-cancerous progression.

Notably, the prognostic associations of *SEMA3C* should be interpreted with caution, as previous studies across the semaphorin family have reported cancer-type-dependent and occasionally protective survival associations. The present findings therefore position *SEMA3C* as a candidate biomarker whose clinical utility warrants validation in cancer-type-specific cohorts.

Future studies employing cell-specific knockout or gain-of-function models, pharmacological blockade of SEMA3C-NRP2 signaling in dietary or fibrogenic injury settings will be essential to establish the *in vivo* causal role of *SEMA3C*. Given the rising NAFLD pandemic, stage-specific evaluation of *SEMA3C* across the steatosis-to-NASH-to-fibrosis spectrum, together with its correlation with metabolic parameters such as insulin resistance and dyslipidemia, would clarify its mechanistic placement within NAFLD-related inflammation. Emerging delivery platforms, such as nanoparticles or MSC-derived exosomes, may ultimately provide translatable strategies for *SEMA3C* inhibition in fibrosis and stroma-rich tumors.

5. Limitations

While our findings provide some insights, certain limitations inherent to the study design should be noted. First, while our *in vitro* experiments in LX-2 cells supported a pro-fibrotic role for *SEMA3C*, the study lacks *in vivo* validation using genetic knockout or pharmacological inhibition in animal models of liver fibrosis. However, *SEMA3C* expression was examined *in situ* in human clinical specimens (qPCR and immunohistochemistry) together with mouse and rat liver fibrosis models (immunofluorescence), which partially remedies this limitation by showing a conserved pattern of *SEMA3C* upregulation; cell-type-specific localization was assessed only in the rodent models and could not be evaluated in human tissue. Second, the pan-cancer analyses depend on retrospective data from public databases, and the estimation of CAF infiltration relies on deconvolution algorithms rather than direct single-cell sequencing. Third, although we identified macro-level stromal associations and enriched signaling pathways, detailed experiments are required to definitively establish the specific receptor complexes mediating *SEMA3C* signaling in HSCs and CAFs. Fourth, the human tissue cohorts were defined by histological diagnosis: numerical fibrosis stage scores were not available for individual TMA cores and the etiology of the TMA cases was not annotated, while the clinical cirrhosis cohort was of mixed etiology and was not stratified by stage or etiology, so the present findings could not be evaluated across individual fibrosis stages or etiological subtypes.

6. Conclusions

In conclusion, this study identifies *SEMA3C* as a critical stromal regulator driven by genetic and epigenetic alterations, deeply involved in both liver fibrosis and pan-cancer microenvironmental remodeling. Through its association with HSCs activation and CAF infiltration, *SEMA3C* may serve as a potential diagnostic and prognostic biomarker, as well as a candidate therapeutic target for intercepting the inflammation-fibrosis-cancer axis.

Availability of Data and Materials

This study analysed publicly available datasets from the Gene Expression Omnibus (GEO) and The Cancer Genome Atlas (TCGA). All datasets are publicly accessible (GEO: https://www.ncbi.nlm.nih.gov/geo/; TCGA via the UCSC Xena platform: https://xena.ucsc.edu). Additional data supporting the findings of this study are available from the corresponding author on reasonable request.

Author Contributions

XiaZ and XuZ put forth the concept and designed the research study. QH and YH performed the bioinformatic analysis, collected public datasets, and crafted the figures and tables. CL, TS, MW, GG and CN conducted the wet lab experiments and clinical sample validation. JZ performed the western blot and qPCR experiments. RJ performed the histological scoring of the TMA. MF supervised and assisted the bioinformatic analysis and data interpretation. XuZ supervised the project, performed critical revision of the manuscript, verified the raw data, and finalized the manuscript. All authors contributed to editorial changes in the manuscript. All authors read and approved the final manuscript. All authors have participated sufficiently in the work and agreed to be accountable for all aspects of the work.

Ethics Approval and Consent to Participate

The collection and use of human clinical liver specimens in this study were approved by the Medical Ethics Committee of Renji Hospital (KY2016-075-A). Written informed consent was obtained from all participating patients, and the study was conducted in strict accordance with the Declaration of Helsinki. The tissue microarray (LV805a) was obtained as fully de-identified archival material from a commercial supplier and was not collected for the purposes of this study; one of the 80 cases is a 16-year-old male. As the specimens carry no identifiable private information, the use of this material was exempt from additional ethical review by the Ethics Committee of the School

of Basic Medicine and Public Health, Jiangsu University. All animal experimental procedures, including the carbon tetrachloride-induced rodent models, were reviewed and approved by the Institutional Animal Care and Use Committee (IACUC) of Jiangsu University (Approval No. UJS-IACUC-2025031646), and followed the guidelines for the care and use of laboratory animals, including the Ethical Review of Animal Welfare (GB/T 35892-2018) and the Guide for the Care and Use of Laboratory Animals (8th edition, National Research Council). The study was carried out in accordance with the ARRIVE guidelines.

Acknowledgment

We thank our collaborators at Renji Hospital for their contributions to the collection and provision of clinical liver tissue samples.

Funding

This work was funded by National Natural Science Foundation of China (No.82103648), China Postdoctoral Science Foundation (2022M711386), Hong Kong Scholars Program (XJ2022046), Jiangsu Natural Science Research Program for Jiangsu Universities (21KJB320013) and Zhenjiang Science and Technology Planning Project (JC2025023).

Conflicts of Interest

The authors declare no conflicts of interest.

Declaration of AI and AI-Assisted Technologies in the Writing Process

During the preparation of this work, the authors used Gemini to check spelling and grammar. After using this tool, the authors reviewed and edited the content as needed and take full responsibility for the content of the publication.

Supplementary Material

Supplementary material associated with this article can be found, in the online version, at https://doi.org/10.31083/FBL55718.

References

[1] Zamani M, Alizadeh-Tabari S, Ajmera V, Singh S, Murad MH, Loomba R. Global Prevalence of Advanced Liver Fibrosis and Cirrhosis in the General Population: A Systematic Review and Meta-analysis. Clinical Gastroenterology and Hepatology. 2025; 23: 1123–1134. https://doi.org/10.1016/j.cgh.2024.08.020

[2] Feng S, Roll GR, Rouhani FJ, Sanchez Fueyo A. The future of liver transplantation. Hepatology (Baltimore, Md.). 2024; 80: 674–697. https://doi.org/10.1097/HEP.0000000000000873

[3] Kisseleva T, Brenner D. Molecular and cellular mechanisms of liver fibrosis and its regression. Nature Reviews. Gastroenterology & Hepatology. 2021; 18: 151–166. https://doi.org/10.1038/s41575-020-00372-7

[4] Cogliati B, Yashaswini CN, Wang S, Sia D, Friedman SL. Friend or foe? The elusive role of hepatic stellate cells in liver cancer. Nature Reviews. Gastroenterology & Hepatology. 2023; 20: 647–661. https://doi.org/10.1038/s41575-023-00821-z

[5] Neira G, Montiel-Duarte C, Becerril S, Valentí V, Moncada R, Catalán V, et al. FNDC4 regulates TGF-β1-induced hepatic stellate cell activation and liver fibrosis via the AMPK/YAP pathway. Free Radical Biology & Medicine. 2026; 249: 152–164. https://doi.org/10.1016/j.freeradbiomed.2026.03.017

[6] Czochra P, Klopcic B, Meyer E, Herkel J, Garcia-Lazaro JF, Thieringer F, et al. Liver fibrosis induced by hepatic overexpression of PDGF-B in transgenic mice. Journal of Hepatology. 2006; 45: 419–428. https://doi.org/10.1016/j.jhep.2006.04.010

[7] Akkız H, Gieseler RK, Canbay A. Liver Fibrosis: From Basic Science towards Clinical Progress, Focusing on the Central Role of Hepatic Stellate Cells. International Journal of Molecular Sciences. 2024; 25: 7873. https://doi.org/10.3390/ijms25147873

[8] Di X, Li Y, Wei J, Li T, Liao B. Targeting Fibrosis: From Molecular Mechanisms to Advanced Therapies. Advanced Science. 2025; 12: e2410416. https://doi.org/10.1002/advs.202410416

[9] Lee J, Vali Y, Boursier J, Spijker R, Anstee QM, Bossuyt PM, et al. Prognostic accuracy of FIB-4, NAFLD fibrosis score and APRI for NAFLD-related events: A systematic review. Liver International: Official Journal of the International Association for the Study of the Liver. 2021; 41: 261–270. https://doi.org/10.1111/liv.14669

[10] Karsdal MA, Daniels SJ, Holm Nielsen S, Bager C, Rasmussen DGK, Loomba R, et al. Collagen biology and non-invasive biomarkers of liver fibrosis. Liver International: Official Journal of the International Association for the Study of the Liver. 2020; 40: 736–750. https://doi.org/10.1111/liv.14390

[11] Castera L, Friedrich-Rust M, Loomba R. Noninvasive Assessment of Liver Disease in Patients With Nonalcoholic Fatty Liver Disease. Gastroenterology. 2019; 156: 1264–1281.e4. https://doi.org/10.1053/j.gastro.2018.12.036

[12] Gao R, Peng X, Perry C, Sun H, Ntokou A, Ryu C, et al. Macrophage-derived netrin-1 drives adrenergic nerve-associated lung fibrosis. The Journal of Clinical Investigation. 2021; 131: e136542. https://doi.org/10.1172/JCI136542

[13] Chang J, Lan T, Li C, Ji X, Zheng L, Gou H, et al. Activation of Slit2-Robo1 signaling promotes liver fibrosis. Journal of Hepatology. 2015; 63: 1413–1420. https://doi.org/10.1016/j.jhep.2015.07.033

[14] De Minicis S, Rychlicki C, Agostinelli L, Saccomanno S, Trozzi L, Candelaresi C, et al. Semaphorin 7A contributes to TGF-β-mediated liver fibrogenesis. The American Journal of Pathology. 2013; 183: 820–830. https://doi.org/10.1016/j.ajpath.2013.05.030

[15] Li Q, Zhang XX, Hu LP, Ni B, Li DX, Wang X, et al. Coadaptation fostered by the SLIT2-ROBO1 axis facilitates liver metastasis of pancreatic ductal adenocarcinoma. Nature Communications. 2023; 14: 861. https://doi.org/10.1038/s41467-023-36521-0

[16] Fard D, Tamagnone L. Semaphorins in health and disease. Cytokine & Growth Factor Reviews. 2021; 57: 55–63. https://doi.org/10.1016/j.cytogfr.2020.05.006

[17] Bica C, Tirpe A, Nutu A, Ciocan C, Chira S, Gurzau ES, et al. Emerging roles and mechanisms of semaphorins activity in cancer. Life Sciences. 2023; 318: 121499. https://doi.org/10.1016/j.lfs.2023.121499

[18] Zhang B, Qi T, Lin J, Zhai S, Wang X, Zhou L, et al. KLF6-mediated recruitment of the p300 complex enhances H3K23su and cooperatively upregulates SEMA3C with FOSL2 to drive 5-FU resistance in colon cancer cells. Experimental & Molecular Medicine. 2025; 57: 667–685. https://doi.org/10.1038/s12276-025-01424-1

[19] Cao P, Cao F, Shui Z, Zhang X, Lv M, Xu H, et al. Cancer-Associated Fibroblast-Centric Risk Model Predicts Im-

munotherapy Resistance in Pancreatic Cancer and Reveals PLOD2 as a Key Stromal Therapeutic Target. Frontiers in Bioscience (Landmark Edition). 2025; 30: 46316. https://doi.org/10.31083/fbl46316

[20] Liang C, Wang M, Huang Y, Yam JWP, Zhang X, Zhang X. Recent Advances of Small Extracellular Vesicles for the Regulation and Function of Cancer-Associated Fibroblasts. International Journal of Molecular Sciences. 2024; 25: 12548. https://doi.org/10.3390/ijms252312548

[21] Qu YA, Huang JC, Wang ZV, Ferguson AL, Nguyen JMH, Zhang M, et al. Understanding the Cancer-Associated Fibroblast (CAF) and Its Biomarker Fibroblast Activation Protein (FAP), and Aspects in Human Liver Cancer. Frontiers in Bioscience (Landmark Edition). 2025; 30: 44837. https://doi.org/10.31083/FBL44837

[22] Prakash J, Pinzani M. Fibroblasts and extracellular matrix: Targeting and therapeutic tools in fibrosis and cancer. Advanced Drug Delivery Reviews. 2017; 121: 1–2. https://doi.org/10.1016/j.addr.2017.11.008

[23] Peng D, Fu M, Wang M, Wei Y, Wei X. Targeting TGF-β signal transduction for fibrosis and cancer therapy. Molecular Cancer. 2022; 21: 104. https://doi.org/10.1186/s12943-022-01569-x

[24] Ding YF, Wu ZH, Wei YJ, Shu L, Peng YR. Hepatic inflammation-fibrosis-cancer axis in the rat hepatocellular carcinoma induced by diethylnitrosamine. Journal of Cancer Research and Clinical Oncology. 2017; 143: 821–834. https://doi.org/10.1007/s00432-017-2364-z

[25] Oey O, Sunjaya AF, Khan Y, Redfern A. Stromal inflammation, fibrosis and cancer: An old intuition with promising potential. World Journal of Clinical Oncology. 2023; 14: 230–246. https://doi.org/10.5306/wjco.v14.i7.230

[26] Hui DHF, Tam KJ, Jiao IZF, Ong CJ. Semaphorin 3C as a Therapeutic Target in Prostate and Other Cancers. International Journal of Molecular Sciences. 2019; 20: 774. https://doi.org/10.3390/ijms20030774

[27] Peng H, Yang M, Feng K, Lv Q, Zhang Y. Semaphorin 3C (Sema3C) reshapes stromal microenvironment to promote hepatocellular carcinoma progression. Signal Transduction and Targeted Therapy. 2024; 9: 169. https://doi.org/10.1038/s41392-024-01887-0

[28] Liu F, Wu Q, Dong Z, Liu K. Integrins in cancer: Emerging mechanisms and therapeutic opportunities. Pharmacology & Therapeutics. 2023; 247: 108458. https://doi.org/10.1016/j.pharmthera.2023.108458

[29] Tarantino G, Citro V. Liver-spleen axis: Deciphering a crucial crosstalk in non-alcoholic fatty liver disease progression and therapeutic implications. World Journal of Gastroenterology. 2026; 32: 119467. https://doi.org/10.3748/wjg.119467

[30] De Angelis Rigotti F, Wiedmann L, Hubert MO, Vacca M, Hasan SS, Moll I, et al. Semaphorin 3C exacerbates liver fibrosis. Hepatology (Baltimore, Md.). 2023; 78: 1092–1105. https://doi.org/10.1097/HEP.0000000000000407

[31] Zhang S, Wan D, Zhu M, Wang G, Zhang X, Huang N, et al. CD11b+CD43hiLy6Clo splenocyte-derived macrophages exacerbate liver fibrosis via spleen–liver axis. Hepatology. 2023; 77: 1612–1629. https://doi.org/10.1002/hep.32782

[32] Fonseca MT, Moretti EH, Marques LMM, Machado BF, Brito CF, Guedes JT, et al. A leukotriene-dependent spleen-liver axis drives TNF production in systemic inflammation. Science Signaling. 2021; 14: eabb0969. https://doi.org/10.1126/scisignal.abb0969